The Astrophysical Journal, 806:180 (15pp), 2015 June 20 doi:10.1088/0004-637X/806/2/180

ATMOSPHERIC HEAT REDISTRIBUTION AND COLLAPSE ON TIDALLY LOCKED ROCKY PLANETS

Robin Wordsworth
School of Engineering and Applied Sciences, Harvard University Cambridge, MA 02138, USA
Received 2014 December 11; accepted 2015 April 7; published 2015 June 17

ABSTRACT

Atmospheric collapse is likely to be of fundamental importance to tidally locked rocky exoplanets, but it remains understudied. Here, general results on the heat transport and stability of tidally locked terrestrial-type atmospheres are reported. First, the problem is modeled with an idealized three-dimensional (3D) general circulation model (GCM) with gray gas radiative transfer. It is shown that over a wide range of parameters that the atmospheric boundary layer, rather than the large-scale circulation, is the key to understanding the planetary energy balance. Through a scaling analysis of the interhemispheric energy transfer, theoretical expressions for the day–night temperature difference and surface wind speed are created that reproduce the GCM results without tuning. Next, the GCM is used with correlated-*k* radiative transfer to study heat transport for two real gases (CO_2 and CO). For CO_2, empirical formulae for the collapse pressure as a function of planetary mass and stellar flux are produced, and critical pressures for atmospheric collapse at Earth's stellar flux are obtained that are around five times higher (0.14 bar) than previous gray gas estimates. These results provide constraints on atmospheric stability that will aid in future interpretations of observations and exoplanet habitability modeling.

Key words: astrobiology – hydrodynamics – planets and satellites: atmospheres – planets and satellites: physical evolution – planets and satellites: terrestrial planets – radiative transfer

1. INTRODUCTION

M-class (red dwarf) stars comprise around 75% of the total stellar population of the Galaxy (Reid et al. 2000), and are attractive targets in searches for nearby terrestrial planets because of the well-known scaling of transit probability and radial velocity signal with stellar mass and planetary orbit (Seager et al. 2010). Ongoing radial velocity and transit surveys have revealed a number of low-mass exoplanets and planet candidates in the stellar neighborhood over the last decade (Charbonneau et al. 2009; Mayor et al. 2009; Pepe et al. 2011; Tuomi et al. 2012), and future dedicated missions such as TESS and Plato are likely to discover many more. Furthermore, transit spectroscopy studies of low-mass "super-Earth" and "mini-Neptune" planets around M-stars have advanced significantly over the past few years (Bean et al. 2010; Croll et al. 2011; Demory et al. 2012; Kreidberg et al. 2013; Fraine et al. 2014). Hot, close-in planets around M-stars are likely to be the first rocky planets for which transit spectroscopy and phase curve observations are possible, making them particularly important targets for theoretical study (Castan & Menou 2011; Miguel et al. 2011; Selsis et al. 2011; Samuel et al. 2014).

Because of these favorable observational conditions, M-stars are also prime targets in the search for habitable Earth-like[1] planets outside the Solar System. However, if habitable planets around M-stars do exist, they are likely to be very different from Earth. First, M-stars have increased extreme ultra-violet (XUV) emission and coronal mass ejection for a much longer period than G-class (Sun-like) stars (Khodachenko et al. 2007; Lammer et al. 2007; Linsky et al. 2013). This means that planets around them may suffer greatly enhanced atmospheric loss, particularly if they lack a magnetic field in the early stages of their evolution (Lammer et al. 2007; Tian 2009; Cohen et al. 2014). Because the most volatile gases (H_2, N_2, Ar, etc.) will generally degas into a planet's atmosphere rapidly during accretion, they are particularly vulnerable to early loss to space. As a result, wide variations in the initial compositions and total masses of the atmospheres of rocky planets around M-stars should be expected.

The low relative luminosities of M-stars mean that planets orbiting close enough to receive Earth-like fluxes or higher are likely to be in tidally resonant or entirely locked states.[2] This means that in some cases, the atmospheres retained by tidally rocky planets after the initial stage of loss to space will be unstable to collapse on the surface (Kasting et al. 1993). Despite the fundamental importance of this process, it has to date received relatively little theoretical attention. Previous work has addressed the problem using three-dimensional (3D) general circulation models (GCMs) in the context of essentially Earth-like planets (Joshi et al. 1997; Joshi 2003) and higher mass super-Earths (Selsis et al. 2011; Wordsworth et al. 2011). Based on these studies, it was found that the stability of a CO_2 atmosphere is a strong function of (a) the total atmospheric mass, (b) the stellar flux received by the planet, and (c) the radiative transfer model used. Using a GCM with simple gray gas radiative transfer and an Earth-like stellar flux $F_E = 1366$ W m^{-2}, Joshi et al. (1997) found that atmospheres above around 0.03 bar p_{CO_2} were stable. In contrast, Wordsworth et al. (2011) used a GCM with realistic correlated-*k* radiative transfer, and found that for a $2.3r_E$ planet receiving around 30% of Earth's incident stellar flux, atmospheric collapse could occur for p_{CO_2} values as large as 10 bar.

A comprehensive study of parameter space for the general collapse problem has not yet been performed. Castan & Menou (2011) modeled the vapor-equilibrium atmospheres of extremely hot super-Earths using an approach first developed to

[1] We do not attempt to define the term "Earth-like" here, although as a minimum it usually implies a similar planetary mass and received stellar flux.

[2] Recently, Leconte et al. (2015) have argued that atmospheric tides could lead to asynchrounous spin–orbit rotation for some Earth-like planets, as for present-day Venus. However, their analysis applies to planets with thick atmospheres (>1 bar) around higher mass (0.5–0.7 $M_\odot$ or greater) stars than the cases considered here.

study Io (Ingersoll et al. 1985), but did not investigate the transition to uncondensed atmospheres. Heng & Kopparla (2012) used an analytical approach to construct stability diagrams across a range of parameters. However, they did not investigate the role of real gas radiative transfer or the planetary boundary layer (PBL). As will be shown here, both of these processes are critical to understanding atmospheric collapse.

Numerous studies of atmospheric circulation on tidally locked terrestrial planets have also recently been conducted (e.g., Joshi 2003; Merlis & Schneider 2010; Heng & Vogt 2011; Pierrehumbert 2011b; Edson et al. 2012; Leconte et al. 2013; Yang et al. 2013). These studies have elucidated several dynamical and climatic processes that are likely to be important in the tidally locked regime (see Showman et al. 2013 for an overview). However, most of them focused on atmospheres with 1 bar surface pressure and Earth-like composition.[3] Because of the uncertainties in volatile delivery and atmospheric erosion, there is no justification for assuming that Earth-mass planets will possess Earth-like atmospheres (or oceans) in general. Hence study of a wider range of scenarios is necessary.

Understanding atmospheric heat redistribution and collapse is particularly important in the context of future spectral observations of rocky planets. This is true both for transiting planets, and potentially for non-transiting cases if phase curve information can be derived (Selsis et al. 2011). Given the complexity of modern GCMs, however, improvements in modeling accuracy must be balanced by advances in basic theory if insight from future observations is to be maximized.

Here a general study of atmospheric stability for tidally locked planets around M-stars is conducted. First, idealized gray-gas GCM simulations are used to study the problem of heat redistribution from day to night side. It is shown that in the physically important limit of slowly rotating optically thin atmospheres, the nightside surface temperature can be estimated analytically, without recourse to any parameters derived from the GCM simulations. Next, the GCM is run in multiband correlated-k mode and used to study collapse across a range of stellar fluxes, atmospheric pressures, and planetary masses. I focus on pure CO_2 compositions but also study one case where CO is the condensing gas. These gases were chosen because they are common products of volcanic outgassing or thermochemistry following bolide impacts but are not easily destroyed via photolysis[4] or lost to space, unlike, e.g., H_2O or CH_4. It is found that the properties of the PBL are more important to the day–night temperature difference than details of the large-scale circulation over wide parameter ranges. In addition, it is shown that the radiative properties of the condensing gas are a key determinant of nightside temperature, and hence the collapse pressure.

In Section 2, the method used for the 3D simulations is described. In Section 3 the idealized gray gas simulations are first presented. Next, a simple theoretical model is used to calculate the nightside surface temperatures produced by the GCM from first principles. Finally, correlated-k GCM results are presented and used to construct simple empirical formulae for the onset of atmospheric collapse for CO_2 and CO as a function of stellar flux, total atmospheric pressure, and planetary mass. In Section 4 the broader implications of the results are discussed and suggestions for future work are given.

Table 1
Standard Parameters Used in the Main Correlated-k GCM Simulations

Parameter	Values
Stellar luminosity L ($L_\odot$)	0.024
Stellar spectrum	AD Leo
Orbital eccentricity e	0.0
Obliquity ϕ	0.0
Atmospheric pressure p (bar)	0.01–10.0
Stellar flux F (1366 W m^{-2})	0.2–3.0
Planet mass M ($M_\oplus$)	1.0, 10.0
Planet radius r ($r_\oplus$)	1.0, 1.88
Surface gravity g (m s^{-2})	9.8, 27.8
Surface roughness height z_0 (m)	1×10^{-2}
Surf. therm. inertia $\mathcal{I}$ (tiu)	250
Surface albedo A	0.2
Atmospheric composition	CO_2, CO

Note. Planet radius and surface gravity r, g were derived from mass M using the scaling relation of Sotin et al. (2007) for rocky planets.

2. METHOD

For the 3D GCM simulations, the Laboratoire de Météorologie Dynamique (LMD) Generic Model is used (Wordsworth et al. 2011, 2013; Forget et al. 2013; Charnay et al. 2013). The key model parameters are shown in Table 1. The LMD model solves the primitive equations on the sphere using the finite-difference approach, with a correlated-k approach for the radiative transfer (Goody & Yung 1989; Wordsworth et al. 2010a). In all simulations, a spatial resolution of 64 × 48 × 18 longitude-latitude-altitude was used, with scaled σ-coordinates in the vertical as in Wordsworth et al. (2013) and a top-of-atmosphere pressure of between 2 and 200 Pa, depending on the surface pressure. The scaled σ-coordinate approach uses constant σ intervals in the high atmosphere but increases resolution near the surface, which increases model stability and permits more accurate resolution of the PBL.

High-resolution line absorption data for input to the correlated-k model was produced using the open-source software *kspectrum* and the HITRAN line database (Rothman et al. 2013). Use of the HITEMP linelist was considered, but comparison of the absorption spectra for HITRAN and HITEMP over the composition, temperature and pressure range of interest indicated that even at the highest temperatures studied here (~550 K), the extra opacity would not significantly alter the results. CO_2 collision-induced absorption was included using the GBB parameterisation (Gruszka & Borysow 1998; Baranov et al. 2004; Wordsworth et al. 2010a), with extrapolation of the data used at temperatures above 400 K. Line-by-line data were then converted to correlated-k format on a 14 × 9 temperature-log pressure grid ranging from 100 to 500 K and 10^{-3} to 10^5 mbar. There were 38 × 36 bands in the infrared and visible, and 16 points were used for the g-

[3] Recently, Wang & Read (2014) and Kaspi & Showman (2014) used a GCM to simulate changes in circulation for a range of parameters, including surface pressure. However, they focused on planets with zonally symmetric average insolation patterns, which are much less vulnerable to atmospheric collapse than the cases we study here.

[4] CO_2 photolyzes to CO and O, which can lead to mixed CO/O_2 atmospheres, but catalytic processes prevent this from happening in the atmospheres of Mars and Venus (Yung et al. 1999). The collapse behavior of pure O_2 or N_2 should be broadly similar to that of CO, except that for these gases, collision-induced absorption is the only source of infrared opacity (Frommhold 2006).

space integration. In all cases the surface topography is assumed to be flat. All simulations were performed assuming a single-component ideal gas atmosphere, with atmospheric condensation represented as in Wordsworth et al. (2010b). For CO_2, the condensation temperature in K was computed as a function of pressure p in Pa as

$$T_{\mathrm{cond,CO_2}} = \frac{-3167.8}{\ln[0.01p] - 23.23} \quad (1)$$

for pressure less than the CO_2 triple-point value ($p < 518000$ Pa) and

$$T_{\mathrm{cond,CO_2}} = 684.2 - 92.3 \ln[p] + 4.32 \ln[p]^2 \quad (2)$$

for higher pressures (Fanale et al. 1982; Wordsworth et al. 2010b). For CO, the vapor-pressure curve was computed using a Clausius–Clayperon ideal gas relation, with parameters derived from Lide (2000). Surface horizontal heat transport (due to, e.g., the presence of an ocean) is also neglected. Both simplifications are chosen to make the problem more tractable, but they also allow a conservative upper limit on the critical collapse pressure.[5] Unlike in Wordsworth et al. (2011), cloud radiative forcing is also neglected. The likely effects of cloud and aerosol radiative forcing are discussed in Section 4. The surface albedo A is taken to be 0.2, a representative value for rocky planets. For the M-star properties, including the stellar spectrum, data for AD Leo (Gliese 388) is used, as in previous studies (Segura et al. 2003; Wordsworth et al. 2010b). AD Leo is highly active in the XUV and undergoes frequent flaring events (Shkolnik et al. 2009), but these properties do not concern us here as we are focused on radiative processes in the lower atmosphere. Rayleigh scattering is included as in Wordsworth et al. (2010a), although its effects are limited around M-stars because of their redshifted spectra. The planetary orbit is assumed to be circular and the obliquity is set to zero (Heller et al. 2011). In all simulations the model was run until thermal equilibrium was reached. Complete tidal locking is assumed, allowing the rotation rate Ω to be calculated from orbital distance via Kepler's third law as

$$\Omega = \frac{2\pi}{1\ \mathrm{year}} \left(\frac{M}{M_\odot}\right)^{1/2} \left(\frac{L}{L_\odot}\right)^{-3/4} \left(\frac{F}{F_E}\right)^{3/4}. \quad (3)$$

Here M, L, and F, are stellar mass, stellar luminosity, and stellar flux incident on the planet, with $M_\odot$, $L_\odot$, and F_E solar and terrestrial values, respectively. Given $L = 0.024 L_\odot$ and $M = 0.4\, M_\odot$ (Pettersen & Coleman 1981; Reiners et al. 2009), (3) can be written as

$$\Omega = 9.2 \times 10^{-9} F^{3/4}. \quad (4)$$

Hence even a planet close enough to receive a stellar flux of $2F_E$ (2732 W m^{-2}) around a typical M-dwarf rotates 20 times less rapidly than Earth. This is the key reason why the effects of rotation on atmospheric circulation are far less important for Earth-like planets around M-stars than for Earth.

For the PBL, the Mellor–Yamada parameterization is used (Mellor & Yamada 1982), with the modifications proposed by Galperin et al. (1988) included. This scheme is known to perform well under most conditions in the Martian atmosphere (Haberle et al. 1993; Forget et al. 1999), which has several similarities to the cases studied here. In brief, the Mellor–Yamada/Galperin (MYG) scheme represents turbulent exchange of momentum and heat between the atmosphere and surface using a 2.5-level closure for the Reynolds-averaged equations. Turbulent kinetic energy q is calculated prognostically assuming a balance between production (via either buoyancy-driven convection or shear in the large-scale flow) and dissipation. Vertical exchange coefficients in the atmosphere and bulk exchange coefficients at the surface are then calculated using q, the potential temperature gradient $\partial\Theta/\partial z$, the turbulence mixing length l and empirical dimensionless constants derived from experimental data (Mellor & Yamada 1982). The turbulence mixing length is calculated from the empirical scaling law of Blackadar (1962)

$$l = \frac{l_0 \mathcal{K} z}{\mathcal{K} z + l_0} \quad (5)$$

where $\mathcal{K} = 0.4$ is the von Kármán constant and l_0 is the maximum attainable mixing length in the boundary layer.

Turbulent exchange coefficients are calculated for every grid point at every time step. Then, the vertical atmospheric diffusion of horizontal momentum and potential temperature are calculated as

$$\left.\frac{\partial \boldsymbol{u}}{\partial t}\right|_{\mathrm{turb}} = \frac{\partial}{\partial z}\left(K_M \frac{\partial \boldsymbol{u}}{\partial z}\right) \quad (6)$$

and

$$\left.\frac{\partial \Theta}{\partial t}\right|_{\mathrm{turb}} = \frac{\partial}{\partial z}\left(K_H \frac{\partial \Theta}{\partial z}\right) \quad (7)$$

given time t, vertical height z, horizontal velocity vector $\boldsymbol{u} = (u, v)$, potential temperature Θ, and momentum and heat eddy diffusion coefficients K_M and K_H, respectively. Diffusion coefficients are calculated using Monin–Obukhov scaling (Garratt 1994) in terms of q, l and the gradient Richardson number, which is defined as the ratio of potential to kinetic energy in the mean flow

$$\mathrm{Ri} = \frac{g}{\Theta}\frac{\partial \Theta}{\partial z}\left[\left(\frac{\partial u}{\partial z}\right)^2 + \left(\frac{\partial v}{\partial z}\right)^2\right]^{-1}. \quad (8)$$

In discrete form, a bulk Richardson number can also be defined as

$$\mathrm{Ri}_B = \frac{g \Delta\Theta/\Theta}{|\boldsymbol{u}|^2/\Delta z}, \quad (9)$$

where Δz is the height from the surface and $\Delta\Theta$ is the potential temperature difference between the surface and the atmospheric region under consideration. In practice, eddy diffusion is high across extended regions of the atmosphere when the Richardson number is low (unstable convective regime), and low outside of a very thin boundary layer region when the Richardson number is high (stable stratified regime).

[5] Neglecting non-condensing background gases is conservative primarily because they pressure-broaden absorption lines of active gases, which increases the atmospheric infrared opacity and warms the planet. However, the redshifted light from M-stars is not strongly affected by Rayleigh scattering, so adding background gases has little direct effect on planetary albedo [e.g., von Paris et al. 2010; Wordsworth et al. 2010b.]

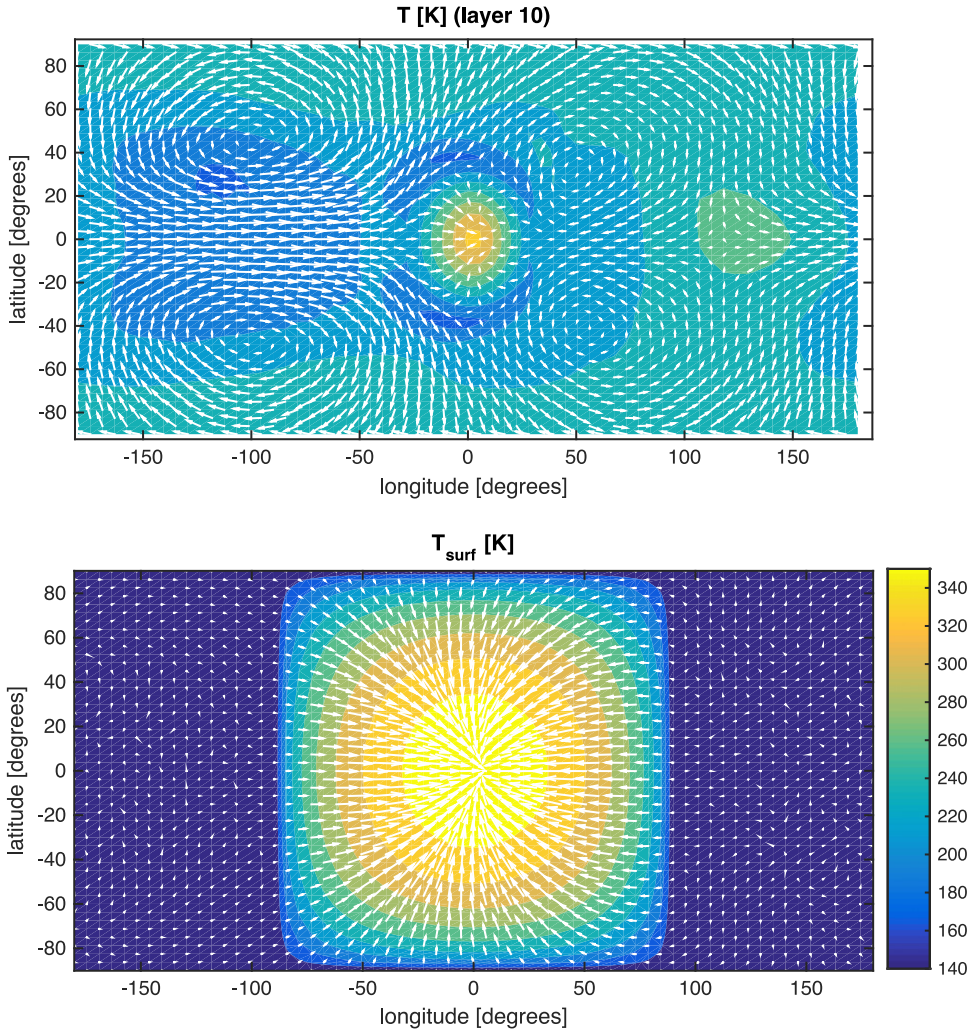

Figure 1. Time-averaged temperature (color contours) and wind (black arrows) in the 0.1 bar gray gas simulation at pressure level $p \approx 0.5p_s$ (top) and at the surface. Some arrows have been removed from the wind fields for clarity.

At the surface, bulk exchange is calculated as

$$\mathcal{F}(f) = C_D \rho_a |\boldsymbol{u}| (f_a - f_s), \tag{10}$$

where $\mathcal{F}$ is the flux of quantity f, C_D is the bulk drag coefficient, and ρ_a and $|\boldsymbol{u}|$ are the atmospheric density and wind speed in the first atmospheric layer, respectively. f_a and f_s are the values of f in the first atmospheric layer and at the surface, respectively; for $f = |\boldsymbol{u}|$, $f_s = 0$. Finally, the bulk drag coefficient is calculated as

$$C_D = \left(\frac{\mathcal{K}}{ln[z/z_0]} \right)^2, \tag{11}$$

where z_0 is the roughness height. z_0 is essentially a free parameter in an exoplanet context, although it can be constrained for terrestrial planets based on solar system radar observations (e.g., Downs et al. 1975; Head et al. 1985; Rosenburg et al. 2011). Here we adopt a representative value for rocky surfaces (Table 1). Note that the dependence of C_D on z_0 is weak, so even order of magnitude variations in roughness length have only a limited effect on the boundary layer behavior (Wordsworth et al. 2011).

3. RESULTS

3.1. Idealized 3D GCM Simulations

To begin the investigation, we examine idealized 3D simulations where gray gas radiative transfer is assumed and the atmospheric extinction of incoming starlight is neglected. Three surface pressures are used: 0.01, 0.1, and 1 bar. The gas is assumed to have the thermodynamic properties of CO_2, with the exception that atmospheric condensation is (for the moment) neglected. Earth radius $r_p = r_E$, gravity $g = g_E$, and incoming stellar flux $F = F_E = 1366$ W m^{-2} are assumed. With a hemispheric mean approximation for the two-stream radiative transfer, total optical depth is

$$\tau = \frac{\kappa p_s}{g \overline{\cos \alpha}}, \tag{12}$$

with p_s surface pressure, g gravity and $\overline{\cos \alpha} = 0.5$ the mean cosine of infrared emission angle. We set $\kappa = 5.0 \times 10^{-5}$ m^2 kg^{-1}, yielding $\tau = 0.1$ at 0.1 bar, which places us in an optically thin radiative regime for two of the three simulations. As will be seen, this is the most relevant limit to study for most (but not all) situations where collapse may occur.

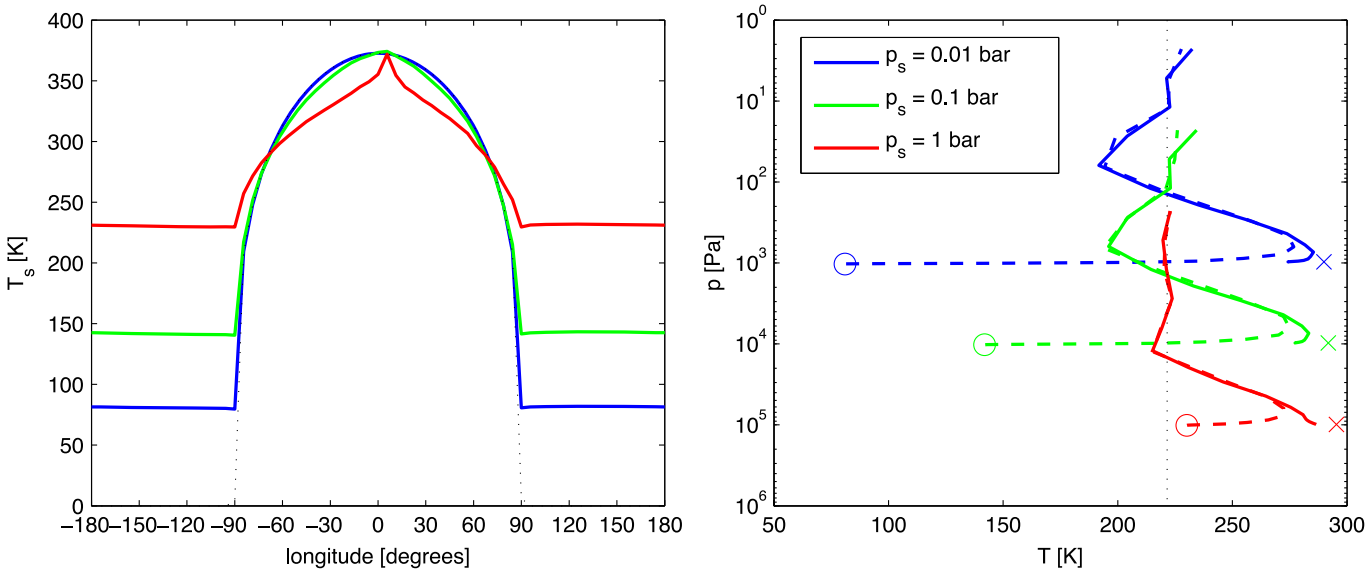

Figure 2. (Left) Time-averaged equatorial surface temperatures in the gray gas simulations. The dotted black line indicates equilibrium temperature. (Right) Hemisphere and time-averaged dayside (solid lines) and nightside (dashed lines) temperature vs. pressure in the same simulations. Crosses and circles indicate dayside and nightside surface temperatures, respectively. The dotted black line indicates skin temperature.

Figure 1 shows the modeled temperatures and winds for the intermediate $p_s = 0.1$ bar simulation both at the surface and in the bulk atmosphere ($p \approx 0.5p_s$). The picture at the surface is a familiar one: a large thermal gradient on the dayside and almost uniform, low temperature on the nightside, with converging surface winds near the substellar point. In the atmosphere, horizontal temperature gradients are *much* lower, and the flow does not show strong superrotation, indicating the limited effect of planetary rotation. This is expected based on a dimensional analysis: the ratio of the equatorial Rossby deformation radius[6] to the planetary radius

$$\frac{L_{\rm Ro}}{r_p} = \sqrt{\frac{R}{c_p}\frac{\sqrt{c_p T_e}}{2\Omega r_p}} \tag{13}$$

is 2.06, suggesting a dynamical regime where rotation has little effect on the large-scale circulation (Leconte et al. 2013). In (13), R and c_p are the specific gas constant and specific heat capacity at constant pressure (for CO_2 here), r_p is planetary radius and $T_e = [(1-A)F/4\sigma]^{\frac{1}{4}}$ is the global equilibrium temperature.

Figure 2 (left) shows the surface temperature at the equator for all simulations as a function of longitude. The dayside temperature is extremely close to the local equilibrium temperature (dotted black line) in the 0.01 and 0.1 bar cases, with some deviations occurring at 1 bar. This indicates that the thermal energy transported to the nightside is generally a small fraction of the total received by the dayside—a fact we will exploit when developing the analytical model in the next section.

Figure 2 (right) shows the day and nightside averaged vertical temperature profiles in the three simulations. All profiles approach the skin temperature $T_{\rm skin} = 2^{-1/4}T_e$ at low pressures, as is expected given the gray radiative transfer. Remarkably, atmospheric temperatures vary little between day and night hemispheres until extremely close to the surface, despite the large differences in day and night surface temperatures. This general feature of tidally locked terrestrial planet atmospheres, which has been noted previously (e.g., Merlis & Schneider 2010; Pierrehumbert 2011b), indicates that they are in a weak temperature gradient (WTG) regime (Sobel et al. 2001; Showman et al. 2013).

This can also be seen from Figure 3, which shows longitude-pressure plots of mean atmospheric temperature and potential temperature for the $p_s = 0.1$ bar case. Potential temperature Θ is related to temperature T as $\Theta = T(p_s/p)^{R/c_p}$, where p and p_s are the atmospheric and surface pressure, respectively. On the dayside near the substellar point, the potential temperature is constant to low pressures (high altitude), indicating an extended convective layer driven by the stellar flux. Outside this region, however, potential temperature varies little with longitude.

To gain further insight into the planetary energy balance, we next study the surface sensible and radiative heat balance. Figure 4 shows a plot of net sensible heat flux, absorbed stellar radiation, and downward/upward infrared radiative fluxes at the surface as a function of longitude for all three simulations. The upwards infrared flux closely matches the absorbed stellar radiation in the 0.01 and 0.1 bar simulations. The downwards infrared radiation is almost constant in all cases, because the atmospheric temperature varies little with longitude. The sensible heat flux is the most interesting: it exhibits a double-peaked structure on the dayside but drops to close to zero on the nightside.

The behavior of the sensible heat flux is a natural consequence of dry boundary layer physics, as captured by the MYG scheme in the model. On the dayside, fluxes are large because the high stellar energy input to the surface creates an intense, permanent convection layer. In this case, the bulk Richardson number Ri_B is extremely low and hence the drag coefficients in (7)–(10) are large, leading to efficient thermal

[6] Note that depending on whether the definition $L_{\rm Ro} = (\sqrt{gH_s}/\beta)^{1/2}$ or $L_{\rm Ro} = (NH_s/\beta)^{1/2}$ is used, with β the latitudinal gradient in planetary vorticity and N the Brunt–Väisälä frequency, $L_{\rm Ro}$ can be varied by a factor of two. We use the Leconte et al. (2013) definition here to yield a (conservative) smaller estimate for $L_{\rm Ro}$.

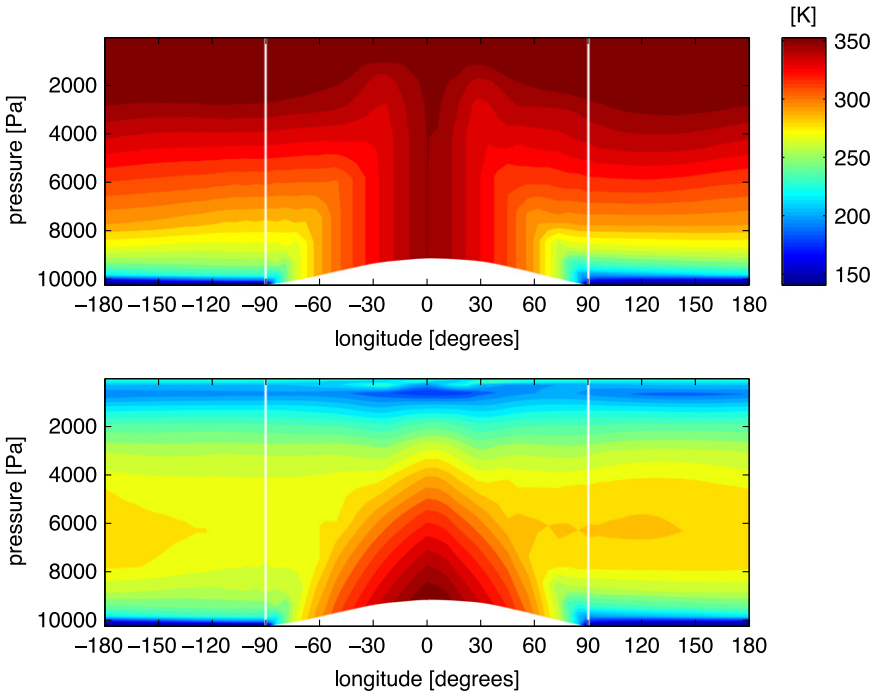

Figure 3. Time-averaged longitude-pressure plots of equatorial potential temperature (top) and temperature (bottom) in the 0.1 bar gray gas simulation. White vertical lines indicate the division between day and night hemispheres.

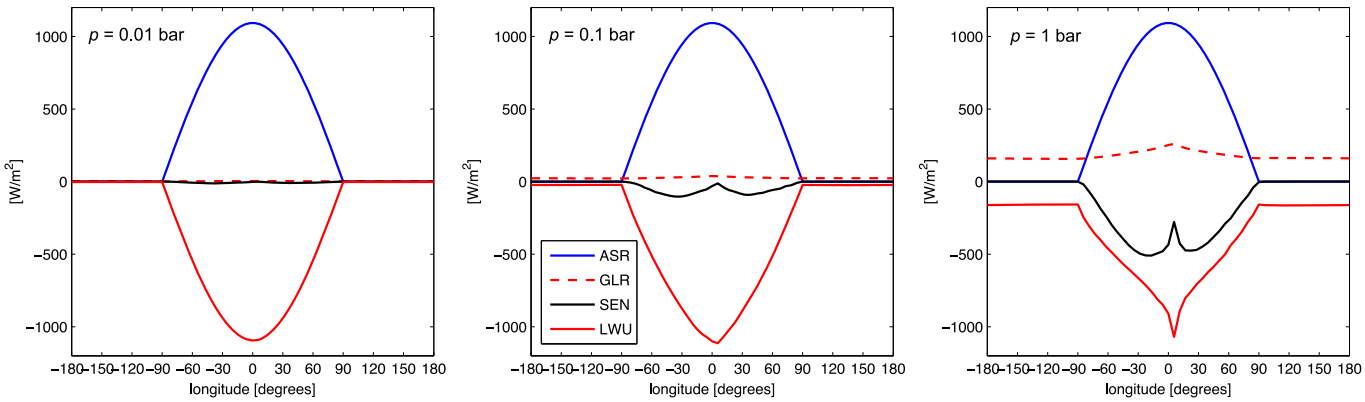

Figure 4. Time-averaged equatorial surface energy balance in the gray gas simulations. ASR, GLR, SEN, and LWU represent absorbed stellar radiation, downwelling infrared (longwave) radiation to the surface, the net sensible heat flux, and the upwelling infrared radiation from the surface, respectively.

coupling with the surface. The double-peaked structure occurs because of the surface wind pattern, which we explore in more detail shortly.

On the nightside, the strong stratification created by the temperature inversion inhibits boundary layer turbulence. The only source of turbulent kinetic energy is the weak large-scale circulation. Mixing is strongly inhibited and the sensible heat flux declines to very low values. A familiar (although less extreme) analogy to this situation is the polar night on Earth. There, radiative cooling to space dominates the surface heat budget, the PBL becomes near-laminar and extremely thin, and the magnitude of the sensible heat flux declines to a low value within days (Cerni & Parish 1984).

To study the large-scale circulation, the wind field output by the model was converted to a coordinate system where the substellar point is a pole. Then, the "meridional" wind component (written here as u_r) represents horizontal motion toward/away from the substellar point. Figure 5 (top) shows the time-averaged surface value of u_r as a function of the stellar zenith angle. The data in Figure 5 was derived by binning the 2D surface u_r fields from the GCM into concentric circles around the substellar point and averaging. All simulations show a minimum (peak inward flow) at around $\theta_z = 40°$, with similar profiles at 0.01 and 0.1 bar and a reduced peak wind speed in the 1 bar case. In all cases the surface wind speed on the nightside ($\theta_z > 90°$) is extremely small. The reduction in wind speed near the substellar point explains the dip in the sensible heat flux there (Figure 4) and hence the sharp peak in surface temperature in the 1 bar case. For the 0.01 and 0.1 bar cases, the sensible heat flux is too low to significantly reduce the dayside surface temperatures.

The 0.1 bar plot of u_r versus θ_z and p (bottom) shows an intense jet (up to 60 m s^{-1}) high in the atmosphere. This is the outward branch of the flow seen near the surface in Figure 1; the wind speed minimum around the $p_s/2$ level indicates the transition between flow to/from the substellar point.

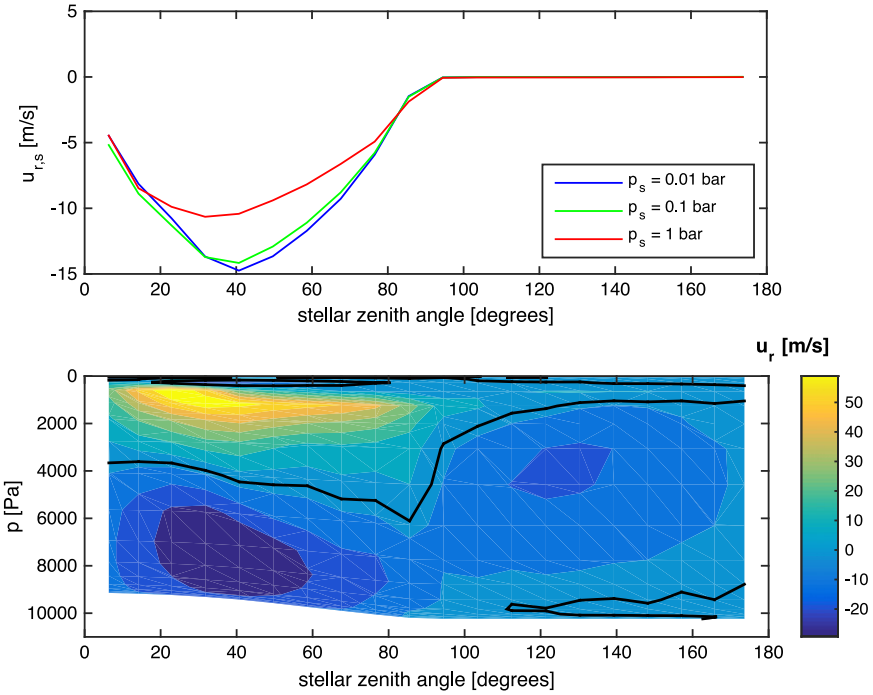

Figure 5. (Top) Mean surface wind component toward/away from the substellar point vs. stellar zenith angle in the gray gas simulations. (Bottom) Mean atmospheric wind component toward/away from the substellar point vs. stellar zenith angle and pressure in the 0.1 bar gray gas simulation. Positive values correspond to flow away from the substellar point. The black line indicates the zero velocity contour.

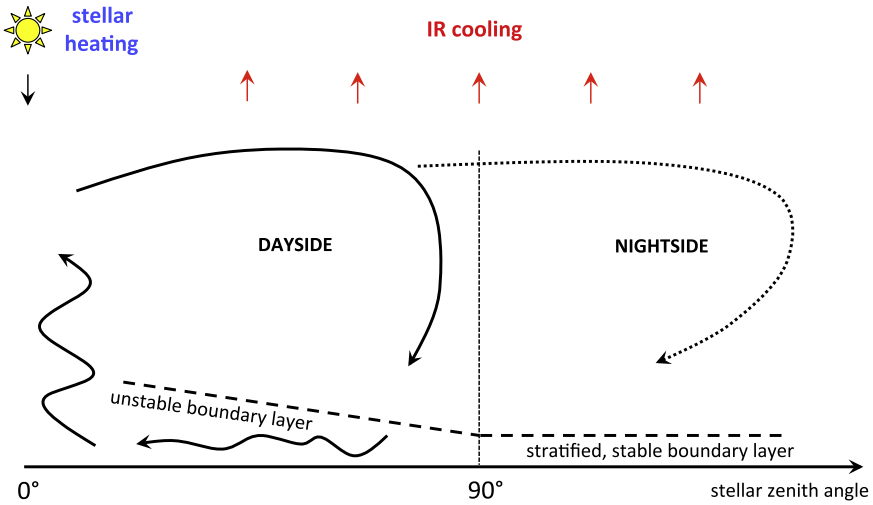

Figure 6. Schematic of key aspects of the circulation and heat transport in a tidally locked atmosphere in contact with a solid surface.

Essentially, when the planetary rotation rate is low, the large-scale circulation has the form of a single planetary-sized convection cell in the dayside, with a slower residual circulation on the nightside (see Figure 6 for a schematic). In the next section, it is shown that the magnitude of the dayside surface wind can be explained by a scaling analysis.

It is interesting to compare the 1 bar, $\tau = 1$ results in Figure 2 (left) with those from the Joshi et al. (1997) study of atmospheric collapse. There, lower day/night side differences were found, with nightside temperatures of around 260–270 K, compared to around 240 K in this study. This suggests that heat redistribution by the atmosphere was much more efficient in their model. The Joshi et al. (1997) model used a simple boundary layer representation based on a quadratic formulation (Joshi et al. 1995), which may have over-represented the efficiency of coupling between the atmosphere and the surface. The subtle issue of accurate sensible heat flux parameterization in the strongly stably stratified regime is discussed further in Section 4.

3.2. Analytical Model

Despite the complexity of the GCM used, the results described in the last section appear essentially simple. To gain a deeper understanding, we now reproduce them using a purely analytical approach. Our goal in this section is to calculate the nightside surface temperature T_n from first principles, without using any GCM-derived coefficients.

To aid development of the model, a schematic of the key features of the circulation is given in Figure 6. Inspired by

Figure 3, we will assume that the atmosphere can be treated as horizontally isothermal outside of the dayside convective zone. This approximation should be applicable as long as the radiative cooling time of a fluid blob transported from the dayside is long compared to the time it takes to be advected. Given this, a three-box model of energy exchange between the dayside surface, atmosphere, and nightside surface can then be constructed. Our approach is somewhat similar to that of Pierrehumbert (2011b) and Yang & Abbot (2014), except here we are after analytical results and hence avoid ad hoc tuning to the GCM simulations.

Given a dry, single-component atmosphere that is transparent in the visible and gray in the infrared and a surface of emissivity equal to 1, the local surface energy balance may be written as

$$\sigma T_s^4 = (1 - A)S\left(\psi, \lambda\right) + \mathrm{GLR} + C_D c_p \rho_a \left|\boldsymbol{u}\right|\left(T_a - T_s\right). \tag{14}$$

Here $S(\psi, \lambda) = F \cos\theta_z$ is the local stellar flux, ψ, λ, and θ_z are longitude, latitude and stellar zenith angle, respectively, GLR is the downwards infrared radiative flux and T_a is the near-surface atmospheric temperature. Similarly, in the absence of visible absorption the vertically integrated local atmospheric energy balance may be written

$$\mathrm{OAR} + \mathrm{GLR} = \mathcal{A}\sigma T_s^4 + \mathcal{D} + C_D c_p \rho_a \left|\boldsymbol{u}\right|\left(T_s - T_a\right), \tag{15}$$

where OAR is the outgoing infrared radiation emitted to space by the atmosphere and $\mathcal{A}$ is the frequency-averaged atmospheric absorptance in the infrared. $\mathcal{D}$ represents the effects of dynamical transport and will disappear once we assume the atmosphere to be isothermal and perform horizontal averaging. The third term on the right hand side of (15) is the sensible heat flux: it is simply (10) with $f = c_p T$ the quantity undergoing exchange.

Next, we define

$$B_d = \frac{\int_d \sigma T_s^4 dA}{2\pi r_p^2} \tag{16}$$

and

$$B_n = \frac{\int_n \sigma T_s^4 dA}{2\pi r_p^2} \tag{17}$$

with $\int_d dA$ and $\int_n dA$ surface integrals over the planet's day and nightsides, respectively. Applying these integrals separately to (14) in turn and averaging (15) over the entire planet, we obtain

$$B_d = \frac{1}{2}(1 - A)F + \mathrm{GLR} + C_D c_p \rho_a \overline{\left|\boldsymbol{u}\right|\left(T_a - T_d\right)}, \tag{18}$$

$$B_n = \mathrm{GLR} + C_D c_p \rho_a \overline{\left|\boldsymbol{u}\right|\left(T_a - T_n\right)}, \tag{19}$$

and

$$\mathrm{OAR} + \mathrm{GLR} = \frac{1}{2}\mathcal{A}B_d + \frac{1}{2}\mathcal{A}B_n + \frac{1}{2}C_D c_p \rho_a \overline{\left|\boldsymbol{u}\right|\left(T_d - T_a\right)} + \frac{1}{2}C_D c_p \rho_a \overline{\left|\boldsymbol{u}\right|\left(T_n - T_a\right)}, \tag{20}$$

where T_d and T_n are the mean dayside and nightside surface temperatures, respectively. Note that because of the isothermal atmosphere assumption, most global average and local atmospheric values are the same (e.g., $\overline{\mathrm{OAR}} = (4\pi r_p^2)^{-1}\int_\Sigma \mathrm{OAR} dA = \mathrm{OAR}$). We allow for the possibility of horizontal variations in $|\boldsymbol{u}|$ and T_d, however, by retaining the overbar for the sensible heat terms.

If the atmosphere can be assumed to be optically thin, $\mathcal{A} \approx \tau$ and $\mathrm{OAR} \approx \mathrm{GLR} \approx \tau B_a$ (Pierrehumbert 2011a). Then (18)–(20) can be simplified to

$$B_d = \frac{1}{2}(1 - A)F + \tau B_a + C_D c_p \rho_a \overline{\left|\boldsymbol{u}\right|\left(T_a - T_d\right)}, \tag{21}$$

$$B_n = \tau B_a + C_D c_p \rho_a \overline{\left|\boldsymbol{u}\right|\left(T_a - T_n\right)}, \tag{22}$$

and

$$4B_a = B_d + B_n + C_D c_p \rho_a \overline{\left|\boldsymbol{u}\right|\left[\left(T_d - T_a\right) + \left(T_n - T_a\right)\right]}\Big/\tau. \tag{23}$$

3.3. Purely Radiative Case

First we examine the artificial but instructive limit where $C_D \to 0$ and the only permitted surface-atmosphere energy exchange is radiative. Then, (21)–(23) reduce to

$$B_d = \frac{1}{2}(1 - A)F + \tau B_a, \tag{24}$$

$$B_n = \tau B_a, \tag{25}$$

and

$$4B_a = B_d + B_n. \tag{26}$$

Hence

$$B_n = \frac{\tau}{2 - \tau}\frac{(1 - A)F}{4}. \tag{27}$$

Because we have already assumed $\tau < 1$, this may be further approximated as

$$B_n \approx \frac{\tau(1 - A)F}{8}. \tag{28}$$

Hence using the definition of optical depth (12) with $\overline{\cos\alpha} = 0.5$,

$$T_n \approx T_{\mathrm{tr}} \equiv \left(\frac{(1 - A)F\kappa p_s}{4\sigma g}\right)^{1/4}. \tag{29}$$

In the thin, isothermal limit with zero sensible heat fluxes, this solves the problem of the surface nightside temperature for a given atmospheric opacity and stellar flux. Note that (29) can

also be derived by neglecting the radiative back-reaction of (a) the atmosphere on the dayside surface and (b) the nightside surface on the atmosphere. In other words, it relies on the assumption that the dayside temperature is unaffected by the presence of an atmosphere, and the atmospheric temperature is unaffected by the heat received from the nightside.

Sticking in the numbers to (29) for the three ideal GCM cases presented in Section 3.1, we get $T_n = 70.4$, 125.2, and 222.7 K for $p = 0.01$, 0.1, and 1 bar, respectively. These values are reasonably close to those calculated by the GCM [see Figure 2 (left)], which is impressive given the simplicity of the derivation. However, there is a systematic bias toward lower temperatures, which is expected given that we are neglecting all turbulent surface-atmosphere heat exchange. I henceforth refer to (29), which provides a lower limit to T_n for optically thin atmospheres, as the *thin radiator temperature*.

3.4. Inclusion of the Dayside Sensible Heat Flux

Now we relax the assumption of zero sensible heat fluxes. It might be tempting to include all terms and attempt to solve (21)–(23) numerically. However, a little more physical insight will allow these equations to be simplified further. Specifically, we invoke the fact that radiative fluxes dominate sensible fluxes in the strongly stratified nightside boundary layer (see Figure 4) and drop terms involving $(T_a - T_n)$ in (22) and (23). We also assume $B_n << B_a$ and $\tau B_a << \frac{1}{2}(1 - A)F$. Hence (21)–(23) become

$$B_d \approx \frac{1}{2}(1 - A)F, \tag{30}$$

$$B_n \approx \tau B_a, \tag{31}$$

and

$$4B_a \approx B_d + C_D g c_p \overline{|\boldsymbol{u}|(T_d/T_a - 1)}\Big/\Big(2\kappa R\Big), \tag{32}$$

where the ideal gas law and (12) have been used. We rewrite $\overline{|\boldsymbol{u}|(T_d/T_a - 1)}$ as $\chi|\boldsymbol{u}|(T_d/T_a - 1)$, where $|\boldsymbol{u}|$, T_d and T_a are now taken to be hemispheric mean values, and χ is a factor that accounts for the fact that temperature peaks at $\theta_z = 0$, whereas $|\boldsymbol{u}|$ peaks around 40°. To this level of approximation we may write $T_d/T_a \propto \cos\theta_z$ and $|\boldsymbol{u}| \propto \sin\theta_z$, yielding $\chi = \int_0^{\pi/2} \cos^2\theta_z \sin\theta_z d\theta_z = 1/3$. By defining a dimensionless atmospheric temperature $\tilde{T} = T_a/T_d$ and velocity $\tilde{U} = |\boldsymbol{u}|/U_0$, with

$$U_0 = (1 - A)F\frac{\kappa}{\chi C_D g}\frac{R}{c_p} \tag{33}$$

we can rewrite (32) as

$$4\tilde{T}^4 - 1 = \tilde{U}\Big(\tilde{T}^{-1} - 1\Big). \tag{34}$$

(34) defines T_a (and hence T_n) as a function of T_d if $|\boldsymbol{u}|$ is known. Note the surface velocity scale U_0 is inversely proportional to the drag coefficient C_D, which is an explicit function of the surface roughness via (11).

3.5. An Equation for $|\boldsymbol{u}|$

To close Equation (34), we next utilize the WTG approximation. WTG scaling for velocity has been analyzed in a shallow water context for Earth (Sobel et al. 2001) and was recently applied to hot Jupiters (Perez-Becker & Showman 2013), suggesting that it should also be useful here. Nonetheless, the central role of the PBL in interhemispheric heat transport on rocky planets means that the approach we take here is rather different from what has been done previously.

The thermodynamic equation (Vallis 2006) is written as

$$\frac{DI}{Dt} + \frac{p}{\rho}\nabla\cdot\boldsymbol{u} = \mathcal{H} \tag{35}$$

with I internal energy, p pressure, ρ density, $\boldsymbol{u}$ velocity, D/Dt the advective derivative, and $\mathcal{H}$ the diabatic heating rate in W kg^{-1}. If the atmosphere is horizontally uniform and flow is steady, this may be simplified to

$$w\frac{dI}{dz} + \frac{p}{\rho}\nabla\cdot\boldsymbol{u} = \mathcal{H}, \tag{36}$$

where z is altitude and w is vertical velocity. For an ideal gas $dI = c_v dT$, with c_v the heat capacity at constant volume. In optically thin atmospheres vertical variation in radiative cooling is low, so we also make the assumption that the lapse rate dT/dz and vertical velocity gradient $\partial w/\partial z$ are small, yielding[7]

$$\nabla\cdot\boldsymbol{u} = \frac{1}{RT_a}\mathcal{H}. \tag{37}$$

Equation (37), which is the essence of the WTG approximation, states that in the absence of time-varying or advective effects, expansion of a fluid column in the bulk atmosphere due to heating must be compensated by outward flow of material to eliminate the horizontal thermal gradient. $\mathcal{H}$ represents the net effect of all heating and cooling processes in a given region. We first focus on the local radiative heating of the dayside atmosphere by the ground $\mathcal{H}_{\mathrm{rad},s} = \kappa\sigma T_d^4 = \frac{1}{2}\kappa(1 - A)F$ to determine the correct scaling.

To achieve this, our strategy is first to switch T_a (which is still unknown) with T_d (which is dependent on the incoming stellar flux and hence is known) in (37). This allows us to create a new velocity scale U_1:

$$\frac{U_1}{L} \sim \frac{1}{RT_d}\mathcal{H}_{\mathrm{rad},s}, \tag{38}$$

$$U_1 \sim \frac{L(1 - A)F\kappa}{2RT_d}. \tag{39}$$

L is a characteristic horizontal length scale that we take here to be the planetary radius r_p. The new velocity scale U_1 may be related to the previously defined surface velocity scale U_0 by writing (39) in terms of the dayside scale height $H_d = RT_d/g$, resulting in

$$U_1 \sim \frac{r_p}{H_d}\frac{(1 - A)F\kappa}{2g}. \tag{40}$$

[7] A more rigorous approach to deriving the WTG approximation would involve integration of (36) in z, accounting for mass conservation and the variation of T and w with height in the entire atmospheric column. We will not pursue this approach here.

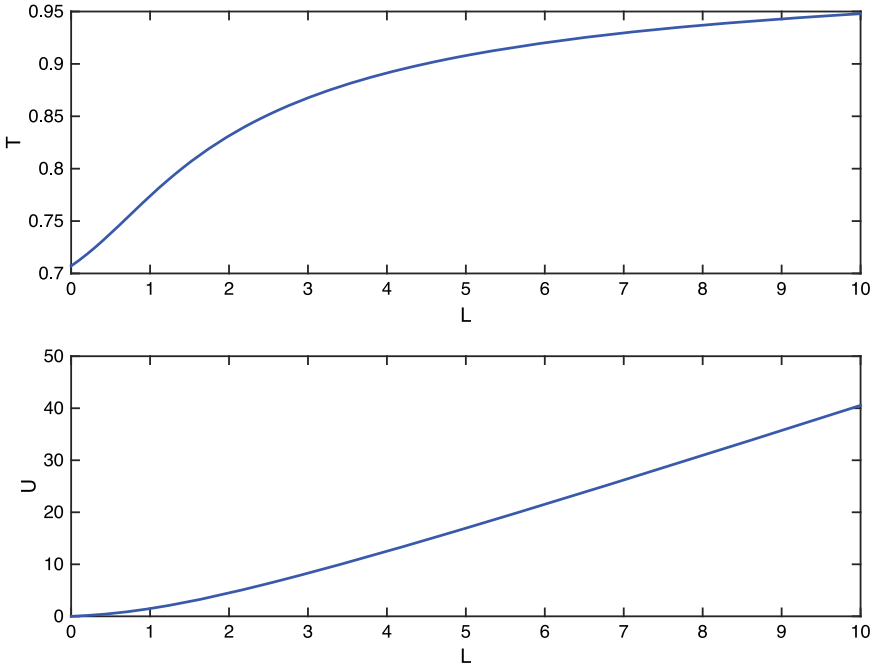

Figure 7. Plot of the dimensionless temperature $\tilde{T}$ (top) and velocity $\tilde{U}$ (bottom) as a function of the dimensionless length $\tilde{L}$.

Finally, defining the dimensionless length scale

$$\tilde{L} = \frac{\chi C_D r_p}{2H_d}\frac{c_p}{R} \tag{41}$$

we can write

$$U_1 \sim \tilde{L} U_0. \tag{42}$$

Given a roughness height of 1×10^{-2} m and height of the first model layer $z \sim 10$ m, $C_D = 0.0034$. For an Earth-mass–planet with CO_2 atmosphere, this yields $\tilde{L} = 2.4$. We shall see that $\tilde{L}$ gives a measure of the strength of $|\boldsymbol{u}|$ and hence of the sensible heat flux from the dayside to the atmosphere.

We now have defined dimensionless temperature, velocity, and length, $\tilde{T}$, $\tilde{U}$, and $\tilde{L}$, and two characteristic velocity scales U_0, U_1 that are related by a factor $\tilde{L}$. Unlike $\tilde{T}$ and $\tilde{U}$, $\tilde{L}$ is a function of external parameters only. We recall that our aim is to solve (34). To do this, the final step is to create an independent equation for $\tilde{U}$ in terms of $\tilde{L}$ and $\tilde{T}$.

We therefore return to (37), write $\nabla \cdot \boldsymbol{u} \sim |\boldsymbol{u}|/r_p$, and now include the dayside radiative cooling and sensible heating terms. This yields

$$\frac{|\boldsymbol{u}|}{r_p} = \frac{1}{RT_a}\left(\kappa\sigma T_d^4 - 2\kappa\sigma T_a^4 + \frac{g\chi C_D\,|\boldsymbol{u}|\,c_p\left(T_d - T_a\right)}{RT_a}\right) \tag{43}$$

with the final term on the right hand side as the sensible heat flux to the atmosphere in W m^{-2} divided by a factor p_s/g to get the heating rate per unit mass. Using the previously derived scaling relations, (43) can now be used to create an expression for the dimensionless velocity

$$\tilde{U} = \frac{\tilde{L}\left(1 - 2\tilde{T}^4\right)}{\tilde{T} + 2\tilde{L}\left(1 - \tilde{T}^{-1}\right)}. \tag{44}$$

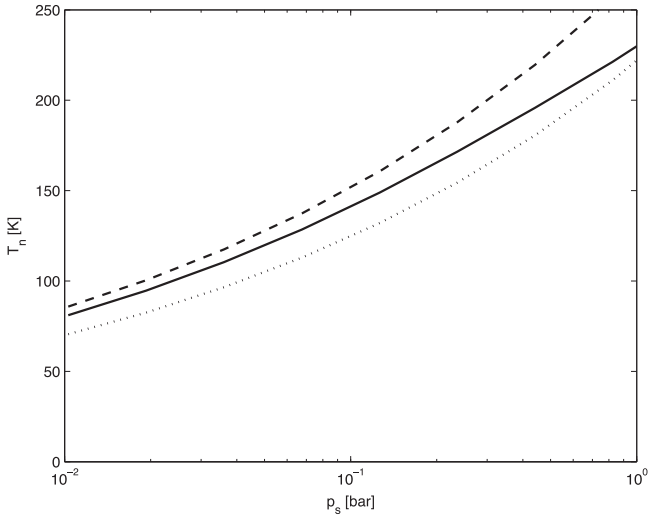

Figure 8. Mean nightside temperature vs. surface pressure in the gray GCM simulations (solid line), predicted by the radiative flux-only analysis (thin radiator temperature; dotted line) and predicted by the radiative + sensible heat flux analysis (dashed line).

Substituting (44) into (34) we finally get

$$\left(4\tilde{T}^4 - 1\right)\left[\tilde{T} + 2\tilde{L}\left(1 - \tilde{T}^{-1}\right)\right] - \tilde{L}\left(1 - 2\tilde{T}^4\right)\left(\tilde{T}^{-1} - 1\right) = 0. \tag{45}$$

This polynomial in $\tilde{T}$ and $\tilde{L}$ can be solved by Newton's method, resulting in expressions for $\tilde{T}$ and $\tilde{U}$ as functions of $\tilde{L}$, which is a fixed parameter for a given planet. The result is shown in Figure 7. Given $\tilde{L} = 2.4$, we find $\tilde{U} = 6.2$ and $\tilde{T} = 0.85$. For $U_0 = 1.2\,\mathrm{m\,s^{-1}}$, $|\boldsymbol{u}| = 7.4\,\mathrm{m\,s^{-1}}$, which is reasonably close to the surface values in Figure 5.

Figure 8 shows the nightside surface temperature predicted by (31) given this result versus gray gas results from the GCM

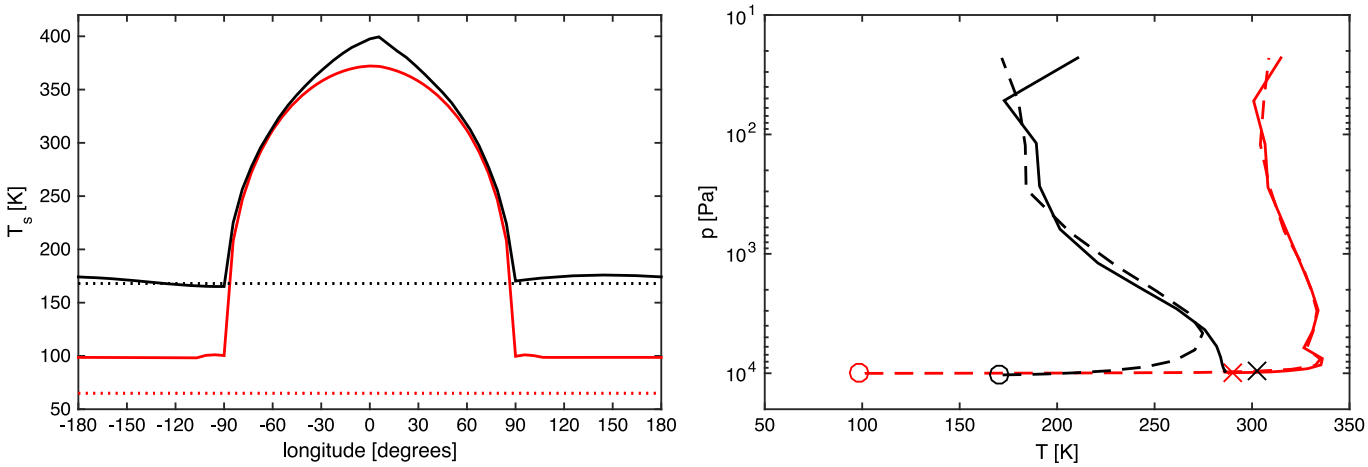

Figure 9. (Left) Time averaged equatorial surface temperatures in the correlated-k simulations for CO_2 (black) and CO (red). The dotted lines indicate the condensation temperature at 0.1 bar for each species. (Right) Hemisphere and time-averaged day and nightside temperatures vs. pressure in the same simulations. Crosses and circles indicate dayside and nightside surface temperatures, respectively.

for a range of surface pressures. As can be seen, the correspondence is close over most of the range of pressures studied, with (31) slightly overpredicting the GCM value of T_n. The "thin radiator temperature" (29) underpredicts the GCM results by a larger margin. The divergence around 1 bar can be explained by the fact that the atmosphere becomes optically thick at that pressure. A similar approach to scaling for the optically thick case should also be possible, and will be addressed in future work.

3.6. Multiband 3D GCM Simulations

Having developed a comprehensive understanding of the key features of interhemispheric heat transport in the gray gas simulations, we now address the full atmospheric collapse problem in the GCM with correlated-k radiative transfer. Figure 9 shows surface and atmospheric temperatures in 0.1 bar GCM simulations with the same planetary parameters as for Figure 3 but using correlated-k radiative transfer and assuming CO_2 (black lines) and CO (red lines) composition. The dotted lines on the left indicate condensation temperatures at 0.1 bar. As can be seen, the nightside is around 70 K colder for CO than for CO_2. Nonetheless, the greater volatility of CO means that it remains stable, whereas in the CO_2 simulation the nightside temperature dips below the condensation temperature.

The inefficient heat transport of the CO atmosphere can be understood by comparing the infrared absorption spectra of CO_2 and CO (Figure 10). As can be seen, the absorption bands of CO_2 are wide and fall near the peak of the Planck function at both 250 and 500 K, while those of CO are thinner and further from the Planck function peak, particularly at low temperatures. The ultimate reason for this is molecular structure: CO is diatomic, with a permanent dipole, and so the infrared absorption spectrum consists of a single weak rotation band at low wavenumbers and a fundamental vibration–rotation band centered at 2143.27 cm^{-1} (Goody & Yung 1989). CO_2, in contrast, has no rotation band due to the lack of a permanent dipole but intense vibration–rotation bands centered on 667 cm^{-1} (15 μm) and 2325 cm^{-1} (4.3 μm) due to the ν_2 and ν_3 fundamental modes, with added absorption due to Fermi resonances, Coriolis interactions, and increased occupancy of higher vibrational levels at moderate temperatures. As demonstrated by the analysis in the preceding sections, the nightside

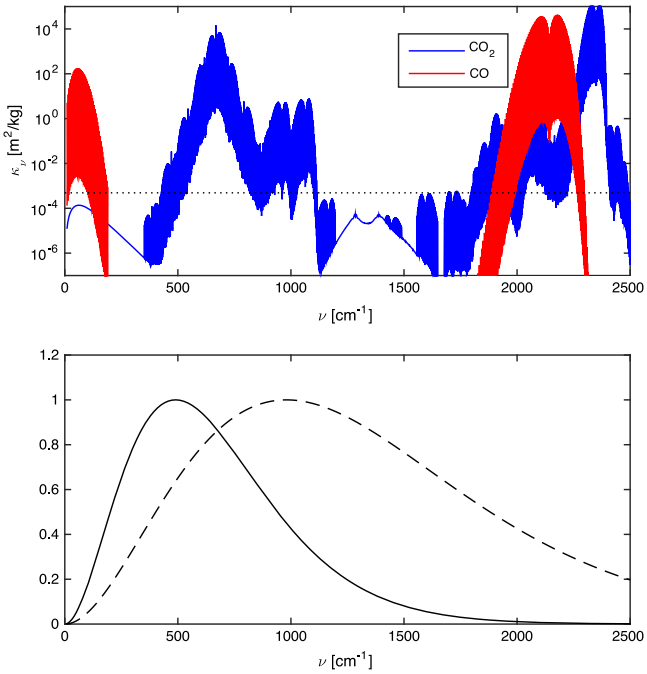

Figure 10. (Top) Infrared mass absorptivity κ_ν of CO_2 and CO at 400 K and 0.1 bar. The black dotted line indicates $\tau = u\kappa_\nu = 1$ for path $u = p_s/g\overline{\cos\alpha} = 2.04 \times 10^3$ kg m^{-2}. CO_2 collision-induced absorption is included for completeness, but its effects are weak at 0.1 bar (Gruszka & Borysow 1997; Baranov et al. 2004; Wordsworth et al. 2010a). (Bottom) Normalized Planck function at 250 K (solid line) and 500 K (dashed line).

temperature depends critically on the atmospheric opacity, and hence weakly absorbing gases cause extremely high surface temperature contrasts. In future observations of hot rocky planets, it should be possible to utilize this effect to constrain atmospheric properties.

The remarkably high *atmospheric* temperatures in the CO case (Figure 10; right) appear paradoxical, but they can also be explained by the radiative properties of the gas. CO is inefficient enough at radiating energy either to space or the surface that almost the entire atmosphere thermally equilibrates with the part of the surface where sensible heat fluxes peak: the dayside near the substellar point. Clearly, if more radiatively active gases or aerosols were present in a CO-dominated

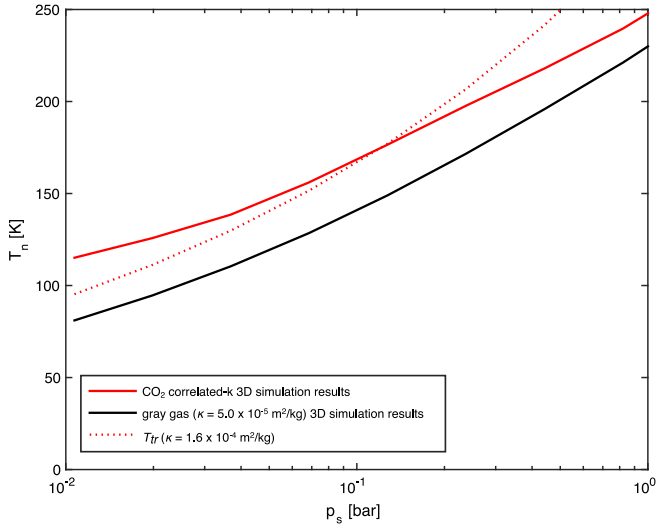

Figure 11. Mean nightside temperature vs. surface pressure in the gray GCM simulations (solid black line), in the correlated-k CO_2 simulations (solid red line), and the thin radiator temperature given $\kappa = 1.6 \times 10^{-4}$ m^2 kg^{-1} (dotted red line).

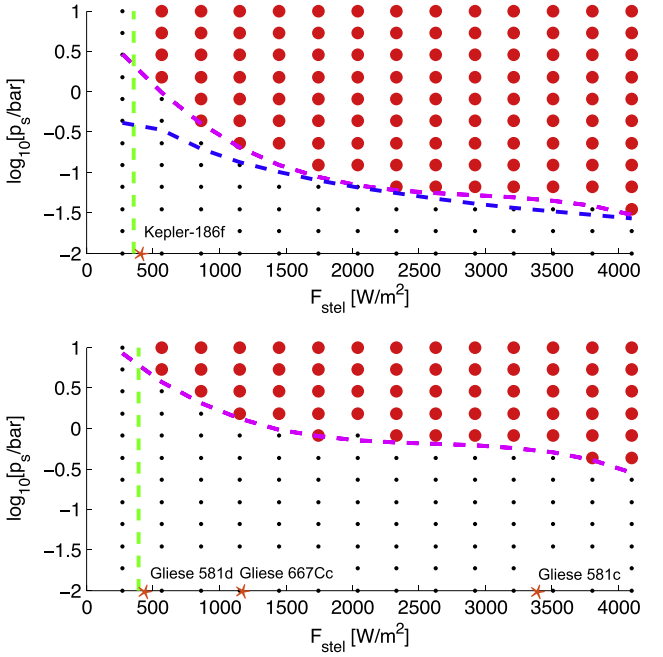

Figure 12. Stability diagram for the CO_2 simulations with correlated-k radiative transfer for a 1 M_E planet (top) and a 10 M_E planet (bottom). Large red dots indicate simulations where the atmosphere remained stable, while small black dots indicate atmospheric collapse. The green dashed line indicates the approximate K–I limit for CO_2, while the magenta dashed line indicates the empirical collapse curve (47) derived from the data. The blue dashed line in the top figure indicates the collapse pressure calculated from the analytic expression (46) with $\kappa = 1.6 \times 10^{-4}$ m^2 kg^{-1}, as described in the text. The orange asterisks indicate the estimated stellar flux received by several exoplanets and exoplanet candidates.

atmosphere even in trace amounts, the behavior of the system could change considerably. Because of the subtlety of this problem, we leave the calculation of collapse pressure for CO and other radiatively inactive, volatile gases such as N_2 to future work.

Figure 11 compares nightside temperature T_n versus surface pressure p_s in the CO_2 correlated-k simulations with the gray gas simulation results displayed in Figure 8. The thin radiator temperature $T_{\rm tr}$ from (29) given a gray atmospheric absorptivity $\kappa = 1.6 \times 10^{-4}$ m^2 kg^{-1} is also plotted. This absorptivity value was chosen to make T_{tr} approximately match the value of T_n produced by the correlated-k simulation at $p_s = 0.1$ bar. As can be seen, the correlated-k simulation yields a less rapid change of nightside temperature with p_s compared to both (29) and the gray gas simulations. This is not surprising, given its strongly non-gray absorption spectrum. A real-gas CO_2 atmosphere radiates heat toward the ground effectively in the 500–700 cm^{-1} spectral region even at very low pressures.

With the atmospheric composition restricted to CO_2 only, condensation was included, and GCM simulations were performed on a 14 × 12 grid in the space of stellar flux and initial atmospheric pressure, for a planet with Earth's mass and radius. Simulations were run for 4 Earth years: at the end, if surface ice was present on the nightside the atmosphere was judged to be in a condensing state. It was not necessary to run the collapsing simulations until they reached thermodynamic equilibrium because collapse is a nonlinear process. As the atmosphere condenses, interhemispheric heat transport decreases, further reducing nightside surface temperatures and accelerating the condensation process.

Figure 12 shows the simulation results. The large red dots show simulations where the atmosphere was stable, while the small black dots show simulations where the atmosphere had begun to condense on the surface. To provide some context, the orange asterisks show the approximate stellar fluxes received by several representative low-mass exoplanets and exoplanet candidates around M-stars (Udry et al. 2007; Anglada-Escudé et al. 2013; Quintana et al. 2014). Finally, the blue dashed line shows the collapse pressure obtained by solving the equation

$$T_{\rm tr}\left(F, p_s\right) = T_{\rm cond,CO_2}\left(p_s\right) \tag{46}$$

at fixed flux F for p_s by Newton's method, with $T_{\rm tr}$ defined by (29), $\kappa = 1.6 \times 10^{-4}$ m^2 kg^{-1}, and $T_{\rm cond,CO_2}$ given by (1).

As can be seen, the onset of atmospheric collapse is a strong function of surface pressure, with collapse occurring for any stellar flux given $p_s < 0.03$ bar. Collapse also occurs at all surface pressures for the lowest stellar flux studied ($0.2\,F_0$ or 273.2 W m^{-2}). These fluxes are below even the values for the exoplanet candidate[8] GJ581d, which we have shown can support stable CO_2 atmospheres above pressures of around 10 bar (Wordsworth et al. 2011). The approximate Kombayashi–Ingersoll limit for CO_2 (Pierrehumbert 2011b) is indicated by the vertical green dashed line.

The analytical results given by the blue line match the empirical curve around $p_s = 0.1$ bar ($\sim F = 1600$ W m^{-2}) by construction, because of our choice of κ in (46). Away from this point, the analytical curve shows the same trend as the numerical results, with a fairly close match at higher stellar fluxes. At low stellar fluxes, the analytical predictions and model results diverge. This is expected, because the theory was developed in the optically thin regime, and the denser atmospheres that undergo collapse at low stellar fluxes are

[8] Although believed to be a real planet by virtually all observational groups for seven years after its discovery (Udry et al. 2007), GJ 581d is now disputed. See the discussions in Baluev (2013), Robertson et al. (2014), and Anglada-Escudé & Tuomi (2015) for details.

Table 2
Coefficients for the Empirical Collapse Equation (47)

Planet mass	c_1	c_2	c_3	c_4
1.0 M_E	-0.84×10^{-10}	0.73×10^{-6}	−0.0022	6.01
10.0 M_E	-0.81×10^{-10}	0.63×10^{-6}	−0.0017	6.34

optically thick. It should be possible to extend the analytical theory to the optically thick regime in future studies.

The prediction of CO_2 collapse at around 0.1 bar contrasts with the results of Joshi et al. (1997), who found that CO_2 atmospheres with pressures as low as 30 mbar would be stable against collapse. There are two reasons for this discrepancy. First, as discussed earlier, Joshi et al. predict somewhat higher nightside temperatures than found here even when we use the same gray gas radiative transfer as they did. Second, models with gray gas radiative transfer significantly overestimate coupling between the atmosphere and nightside surface (Leconte et al. 2013). Particularly at pressures less than 1 bar, windows in the absorption spectrum (e.g., at wavenumbers less than 500 cm^{-1} for CO_2) allow the surface to emit radiation directly to space, greatly increasing cooling rates.

It is also interesting to compare the results given here with the analytical predictions of Heng & Kopparla (2012). Essentially the entire range spanned by Figure 12 is in their predicted "stable atmosphere" region (see their Figure 3), indicating that their $t_{adv} < t_{rad}$ criterion does not represent a sufficient condition for atmospheric stability independent of atmospheric pressure. Conversely, $t_{adv} > t_{rad}$ as they define it does not appear to be sufficient for instability in all cases, because in simulations assuming a 10 $M_\oplus$ planet, stable atmospheric solutions at high CO_2 pressures were also found (Figure 12 (bottom)). In the highly irradiated regime where the flow Mach number can approach the sound speed, however, their approach may still be applicable. Applying 3D circulation models with real gas radiative transfer to this problem will be an interesting topic for future research.

Finally, using the data shown in Figure 12, empirical formulae of the critical collapse pressure p_{crit} versus stellar flux were created according to the expression

$$\log_{10}\left[\frac{p_{crit}}{1\ \mathrm{Pa}}\right] = c_1 F_s^3 + c_2 F_s^2 + c_3 F_s + c_4, \quad (47)$$

with the constants c_i derived by a least-squares fit. The results are shown in Figure 12, with the coefficients given in Table 2.

The atmosphere collapses at higher pressures in general on higher-mass planets for several reasons. First, the increase in gravity means a lower column mass for a given pressure. This means the total atmospheric opacity is also lower, and hence the nightside temperature decreases. In addition, higher planetary radii mean the advection time $t_{adv} = r_p/|\boldsymbol{u}|$ should be smaller if $|\boldsymbol{u}|$ remains constant. However, in the WTG regime the scaling of $\tilde{U}$ with $\tilde{L}$ and hence r_p suggests that this effect should be less important.

The decrease in the critical collapse pressure with stellar flux can be understood by reference to (29). Increasing stellar flux implies a greater amount of heat is transported to the nightside, and hence a lower total pressure can be achieved before collapse occurs. Because at fixed stellar luminosity we increase stellar flux by moving the planet inwards, the effects of rotation on the circulation must eventually become important. However, its importance appears to be secondary for the range of cases studied here.

4. DISCUSSION

Atmospheric collapse is likely to be of fundamental importance for tidally locked rocky planets. The analysis in the preceding section has demonstrated that despite the fact that the collapse problem involves coupling between several complex processes (radiative transfer, the large-scale circulation and boundary layer turbulence), its key features can be understood using an entirely analytical approach.

How robust are these results? Clearly, modifying effects such as ocean heat transport or intense tidal heating of the planetary interior could result in more stable atmospheres than found here. The presence of radiatively active trace gases would also render an atmosphere more stable than the single-component cases studied here by increasing the radiative coupling between the atmosphere and nightside of the planet. A similar role could be played by aerosols released by volcanism or by surface lifting of dust, although maintaining an atmosphere on geological timescales through such a mechanism would be challenging. Clouds can also potentially contribute to greenhouse warming on the nightside, as we found previously for CO_2 in Wordsworth et al. (2011), although the thermodynamics disfavors nightside H_2O cloud formation for Earth-like tidally locked planets (Yang et al. 2013). Further modeling will be required to assess the potential importance of these effects. Most processes will lead to a reduction in the collapse pressure, though, so in this sense the results in Table 2 can be regarded as a conservative upper limit.

Another point worth discussing is the representation of the boundary layer physics in the strongly stratified regime. Evidence from terrestrial observations of nocturnal and polar PBLs indicates that turbulent motion does not cease completely when Ri is greater than the "critical" value of 0.2 (Strang & Fernando 2001; Monti et al. 2002; Galperin et al. 2007). This effect, which can be understood in the context of gravity wave turbulence, is not properly accounted for in the MYG boundary layer scheme. Could it significantly modify the results described here?

Sukoriansky et al. (2005) recently developed a spectral model of stratified turbulent flows that accounts for gravity wave turbulence in the high Ri regime, using a renormalization group approach that progressively replaces the full nonlinear fluid equations at increasing scales by a quasi-Gaussian Langevin equation. They showed that as Ri increases, horizontal eddy viscosities and diffusivities increase, enhancing horizontal mixing. However, vertical eddy viscosity drops to a low (constant) value, while vertical diffusivity declines to zero (Figure 8 in Sukoriansky et al. 2005). At sufficiently high stable stratification, the sensible heat flux should be negligible, even while horizontal mixing remains high. In the 0.1 bar CO_2 simulation in Figure 9 of this paper, the bulk Richardson number Ri_B at the surface is around 1, implying a small addition to the sensible heat flux due to gravity wave turbulence. In future studies it will be interesting to incorporate this effect into the GCM boundary layer scheme. It is likely to be more significant for CO and other highly volatile, radiatively inactive gases than for gases like CO_2.

For potentially habitable planets, this work has several broad implications. Clearly, atmospheric collapse is a vital effect that may be a key driver of climate in some cases. It has been shown that interhemispheric heat transport and hence global climate depends strongly on both total atmospheric pressure and composition—a fact that is often neglected in GCM studies of habitability around M-stars, which currently tend to focus on Earth-like planets only. Here, only CO_2 and CO atmospheres have been studied, to allow a focus on physical processes, but a collapse of other volatiles on a planet's nightside, particularly H_2O (e.g., Menou 2013), may be significant and linked to the overall oxidation rate of the planet (Wordsworth & Pierrehumbert 2014). Future work needs to focus on the efficiency of delivery/loss mechanisms for highly volatile gases (H_2, N_2, Ar, He) on low-mass planets, and coupling between the dynamical processes studied here and atmospheric chemistry, including the overall rate of oxidation via photolysis and hydrogen escape for planets with surface liquid water.

For hotter planets, the theoretical framework developed here should also be applicable. However, in the very close-in, extremely highly irradiated regime a number of additional effects may become important, including more rapid radiative cooling of the atmosphere, Coriolis effects, and increased surface friction. Eventually, there may be a crossover to a regime where a more Io-like circulation (Ingersoll et al. 1985; Castan & Menou 2011) dominates. This will be an important issue to tackle in future work.

Finally, this study has important potential implications for future observations of rocky exoplanets (habitable or not) by ground-based facilities or spacecraft such as the *James Webb Space Telescope*. Most simply, if a given molecule is detected in the transit spectrum of a tidally locked planet, knowledge of that molecule's critical collapse pressure will allow constraints to be placed on the atmospheric composition. Similarly, a rigorous understanding of rocky planet interhemispheric heat transport is necessary for future interpretation of future broadband transit and phase curve data. Finally, as discussed in Selsis et al. (2011), if a planet's variation spectrum can also be retrieved, powerful simultaneous constraints on atmospheric pressure and composition become achievable. Future work will generalize the results presented here to a variety of atmospheric compositions and investigate these issues in greater detail.

This research was partially supported by the National Science Foundation and NASA's VPL program. This article benefited from discussions with many researchers, including Peter Read, Manoj Joshi, François Forget, Zhiming Kuang, and Remco de Kok. The author also thanks the anonymous reviewer for helpful comments that significantly improved the manuscript. The computations in this paper were run on the Odyssey cluster supported by the FAS Division of Science, Research Computing Group at Harvard University.

REFERENCES

Anglada-Escudé, G., & Tuomi, M. 2015, Sci, 347, 1080
Anglada-Escudé, G., Tuomi, M., Gerlach, E., et al. 2013, A&A, 556, A126
Baluev, R. V. 2013, MNRAS, 429, 2052
Baranov, Y. I., Lafferty, W. J., & Fraser, G. T. 2004, JMoSp, 228, 432
Bean, J. L., Kempton, E., & Homeier, D. 2010, Natur, 468, 669
Blackadar, A. K. 1962, JGR, 67, 3095
Castan, T., & Menou, K. 2011, ApJL, 743, L36
Cerni, T. A., & Parish, T. R. 1984, JCAM, 23, 1563
Charbonneau, D., Berta, Z. K., Irwin, J., et al. 2009, Natur, 462, 891
Charnay, B., Forget, F., Wordsworth, R., et al. 2013, JGRD, 118, 10
Cohen, O., Drake, J., Glocer, A., et al. 2014, arXiv:1405.7707
Croll, B., Albert, L., Jayawardhana, R., et al. 2011, ApJ, 736, 78
Demory, B.-O., Gillon, M., Seager, S., et al. 2012, ApJL, 751, L28
Downs, G., Reichley, P., & Green, R. 1975, Icar, 26, 273
Edson, A. R., Kasting, J. F., Pollard, D., Lee, S., & Bannon, P. R. 2012, AsBio, 12, 562
Fanale, F. P., Salvail, J. R., Banerdt, W. B., & Saunders, R. S. 1982, Icar, 50, 381
Forget, F., Hourdin, F., Fournier, R., et al. 1999, JGR, 104, 24155
Forget, F., Wordsworth, R. D., Millour, E., et al. 2013, Icar, 222, 8
Fraine, J., Deming, D., Benneke, B., et al. 2014, Natur, 513, 526
Frommhold, L. 2006, Collision-induced absorption in gases, Vol. 2 (Cambridge: Cambridge Univ. Press)
Galperin, B., Kantha, L. H., Hassid, S., & Rosati, A. 1988, JAtS, 45, 55
Galperin, B., Sukoriansky, S., & Anderson, P. S. 2007, AtScL, 8, 65
Garratt, J. R. 1994, The Atmospheric Boundary Layer (Cambridge: Cambridge Univ. Press)
Goody, R. M., & Yung, Y. L. 1989, in Atmospheric Radiation: Theoretical Basis, ed. M. Richard, Goody, & Y. L. Yung (2nd ed.; New York, NY: Oxford Univ. Press), 1
Gruszka, M., & Borysow, A. 1997, Icar, 129, 172
Gruszka, M., & Borysow, A. 1998, MolPh, 93, 1007
Haberle, R. M., Houben, H. C., Hertenstein, R., & Herdtle, T. 1993, JAtS, 50, 1544
Head, J. W., Peterfreund, A. R., Garvin, J. B., & Zisk, S. H. 1985, JGRB, 90, 6873
Heller, R., Leconte, J., & Barnes, R. 2011, A&A, 528, 27
Heng, K., & Kopparla, P. 2012, ApJ, 754, 60
Heng, K., & Vogt, S. S. 2011, MNRAS, 415, 2145
Ingersoll, A. P., Summers, M. E., & Schlipf, S. G. 1985, Icar, 64, 375
Joshi, M. 2003, AsBio, 3, 415
Joshi, M. M., Haberle, R. M., & Reynolds, R. T. 1997, Icar, 129, 450
Joshi, M., Lewis, S., Read, P., & Catling, D. 1995, JGRE, 100, 5485
Kaspi, Y., & Showman, A. P. 2014, arXiv:1407.6349
Kasting, J. F., Whitmire, D. P., & Reynolds, R. T. 1993, Icar, 101, 108
Khodachenko, M. L., Ribas, I., Lammer, H., Farrugia, C. J., et al. 2007, AsBio, 7, 167
Kreidberg, L., Bean, J. L., Désert, J.-M., et al. 2014, Natur, 505, 69
Lammer, H., Lichtenegger, H. I. M., Kulikov, Y. N., et al. 2007, AsBio, 7, 185
Leconte, J., Forget, F., Charnay, B., et al. 2013, arXiv:1303.7079
Leconte, J., Wu, H., Menou, K., & Murray, N. 2015, Sci, 1, 1258686
Lide, D. P. (ed.) 2000, in CRC Handbook of Chemistry and Physics (81 ed.; Boca Raton, FL: CRC Press)
Linsky, J. L., France, K., & Ayres, T. 2013, ApJ, 766, 69
Mayor, M., Bonfils, X., Forveille, T., et al. 2009, A&A, 507, 487
Mellor, G. L., & Yamada, T. 1982, RvGeo, 20, 851
Menou, K. 2013, ApJ, 774, 51
Merlis, T. M., & Schneider, T. 2010, JAMES, 2, 4
Miguel, Y., Kaltenegger, L., Fegley, B., & Schaefer, L. 2011, ApJL, 742, L19
Monti, P., Fernando, H., Princevac, M., Chan, W., Kowalewski, T., & Pardyjak, E. 2002, JAtS, 59, 2513
Pepe, F., Lovis, C., Segransan, D., et al. 2011, arXiv:1108.3447
Perez-Becker, D., & Showman, A. P. 2013, ApJ, 776, 134
Pettersen, B. R., & Coleman, L. A. 1981, ApJ, 251, 571
Pierrehumbert, R. 2011a, Principles of Planetary Climate (Cambridge: Cambridge Univ. Press)
Pierrehumbert, R. T. 2011b, ApJL, 726, L8
Quintana, E. V., Barclay, T., Raymond, S. N., et al. 2014, Sci, 344, 277
Reid, N., Reid, I. N., Reid, N., & Hawley, S. 2000, New Light on Dark Stars (Berlin: Springer)
Reiners, A., Basri, G., & Browning, M. 2009, ApJ, 692, 538
Robertson, P., Mahadevan, S., Endl, M., & Roy, A. 2014, Sci, 345, 440
Rosenburg, M., Aharonson, O., Head, J., et al. 2011, JGRE, 116, E2
Rothman, L., Gordon, I., Babikov, Y., et al. 2013, JQSRT, 130, 4
Samuel, B., Leconte, J., Rouan, D., et al. 2014, arXiv:1402.6637
Seager, S., Dotson, R., et al. 2010, Exoplanets (Tucson, AZ: Univ. Arizona Press)
Segura, A., Krelove, K., Kasting, J. F., et al. 2003, AsBio, 3, 689
Selsis, F., Wordsworth, R., & Forget, F. 2011, A&A, 532, A1
Shkolnik, E., Liu, M. C., & Reid, I. N. 2009, ApJ, 699, 649
Showman, A. P., Wordsworth, R. D., Merlis, T. M., & Kaspi, Y. 2013, arXiv:1306.2418
Sobel, A. H., Nilsson, J., & Polvani, L. M. 2001, JAtS, 58, 3650
Sotin, C., Grasset, O., & Mocquet, A. 2007, Icar, 191, 337
Strang, E., & Fernando, H. 2001, JPO, 31, 2026
Sukoriansky, S., Galperin, B., & Staroselsky, I. 2005, PhFl, 17, 085107
Tian, F. 2009, ApJ, 703, 905

Tuomi, M., Jones, H. R., Jenkins, J. S., et al. 2012, arXiv:1212.4277
Udry, S., Bonfils, X., Delfosse, X., et al. 2007, A&A, 469, L43
Vallis, G. K. 2006, Atmospheric and Oceanic Fluid Dynamics: Fundamentals and Large-scale Circulation (Cambridge: Cambridge Univ. Press)
von Paris, P., Gebauer, S., Godolt, M., et al. 2010, A&A, 522, A23+
Wang, Y., & Read, P. 2014, in Proc. IAU Symp. 293, Diversity of Planetary Atmospheric Circulations and Climates in a Simplified General Circulation Model (Cambridge: Cambridge Univ. Press), 297
Wordsworth, R., Forget, F., & Eymet, V. 2010a, Icar, 210, 992
Wordsworth, R., Forget, F., Millour, E., et al. 2013, Icar, 222, 1
Wordsworth, R., & Pierrehumbert, R. 2014, ApJL, 785, L20
Wordsworth, R. D., Forget, F., Selsis, F., et al. 2010b, A&A, 522, A22+
Wordsworth, R. D., Forget, F., Selsis, F., et al. 2011, ApJL, 733, L48
Yang, J., & Abbot, D. S. 2014, ApJ, 784, 155
Yang, J., Cowan, N. B., & Abbot, D. S. 2013, ApJL, 771, L45
Yung, Y. L., & DeMore, W. B. 1999, in Photochemistry of Planetary Atmospheres, Vol. 1, ed. Yuk L. Yung, & William B. DeMore (New York: Oxford Univ. Press), QB603